Processing and optimization of patched C/C-SiC plates

Jonas Riesner, Dietmar Koch, Nils Meyer

Angaben zur Veröffentlichung / Publication details:

Riesner, Jonas, Dietmar Koch, and Nils Meyer. 2026. "Processing and optimization of patched C/C-SiC plates." *Composites Part A: Applied Science and Manufacturing* 208: 109890. https://doi.org/10.1016/j.compositesa.2026.109890.

Composites: Part A 208 (2026) 109890

Contents lists available at ScienceDirect

Composites Part A

journal homepage: www.elsevier.com/locate/compositesa

Processing and optimization of patched C/C-SiC plates

Jonas Riesner [a,*], Dietmar Koch [a,b], Nils Meyer [a,b]

[a] University of Augsburg, Institute of Materials Resource Management, Augsburg, Germany
[b] University of Augsburg, Centre for Advanced Analytics and Predictive Sciences, Augsburg, Germany

ARTICLE INFO

Keywords:
Ceramic matrix composites
Fiber Patch Placement
Parameter identification
Optimization
C/C-SiC

ABSTRACT

Fiber Patch Placement is a flexible and efficient manufacturing approach for producing locally reinforced composite structures, enabling precise alignment of unidirectional fiber patches along principal load paths. However, processing and design methods focus primarily on polymer matrix composites without addressing the specific constraints and needs for patched ceramic matrix composites. Therefore, this study presents a novel methodology for processing and optimization of locally reinforced carbon/carbon–silicon carbide (C/C–SiC) manufactured via Liquid Silicon Infiltration. An inverse method is introduced to indirectly identify the anisotropic stiffness properties of unidirectional fiber patches from experiments on cross-ply laminates. Based on these material parameters, a gradient-based optimization framework employing differentiable finite element analysis is developed to determine optimal patch placement for structural reinforcement. The approach is validated on a plate with a central hole under tensile loading, where the optimized patch layout is successfully manufactured using a two-step curing process. The results demonstrate stiffness improvements of up to 59% with a weight increase of only 14%.

1. Introduction

Ceramic matrix composites (CMC), especially carbon/carbon-silicon carbide (C/C-SiC) composites, are high-performance materials used in aerospace, automotive, and energy sectors [1]. Such C/C-SiC composites offer low density, good thermal shock resistance, and improved fracture toughness compared to monolithic ceramics, as along with strong mechanical performance at elevated temperatures [2,3]. These characteristics make them suitable for use in challenging environments where traditional materials may not perform adequately.

A fast and cost-effective method for manufacturing C/C-SiC composites is the three-step process called Liquid Silicon Infiltration (LSI) [2]:

1. A carbon fiber reinforced polymer (CFRP) part is produced in common CFRP-processes such as Resin Transfer Molding (RTM), autoclave processing, or filament winding. The preferred matrix materials are phenolic resins due to their relatively high carbon yield during the subsequent pyrolysis step.
2. The phenolic resin is then transformed into amorphous carbon through pyrolysis at temperatures above 900 °C under an inert atmosphere. The transformation causes a significant mass loss of approximately 50 wt.-% [4] typically causing translaminar segmentation cracks in cross-ply laminates [5].
3. Finally, pores and cracks are filled with liquid silicon at high temperature. The infiltration of liquid silicon occurs via capillary forces. Immediately upon contact with the carbon matrix, a SiC layer forms at the interface. After the silicon infiltration process is complete, any unreacted silicon remains as free silicon within the capillaries.

RTM and autoclave-based processes still require manual lay-up of CFRP preforms. This is especially challenging for complex geometries, as it complicates the draping process and usually leads to significant material waste due to trimming. As fiber production represents a major share of the overall energy consumption in the LSI process, minimizing fiber usage is essential [6]. Load-path optimized design is an effective approach by placing fibers only where they contribute to structural performance. Additionally, a significant reduction of the overall weight can be realized. Achieving such optimized designs requires high flexibility in fiber placement. Automated Tape Laying (ATL) and Automated Fiber Placement (AFP) are established technologies in aerospace manufacturing but face limitations when dealing with small structures, complex fiber orientations, and small curvature radii. A novel method offering greater flexibility is Fiber Patch Placement (FPP). In this approach the structure is assembled from unidirectional, spread fiber patches. Each patch can be arbitrarily oriented, allowing the realization of highly complex fiber architectures.

There are two approaches to manufacturing FPP structures: The first approach involves building a complete laminate entirely from

* Corresponding author.
E-mail address: jonas.riesner@uni-a.de (J. Riesner).

https://doi.org/10.1016/j.compositesa.2026.109890
Received 15 October 2025; Received in revised form 13 April 2026; Accepted 28 April 2026
Available online 2 May 2026

fiber patches. Such patch-based laminates typically consist of several hundred to thousands of individual patches. The second approach uses a significantly lower number of fiber patches, placing them only in critical locations on an existing base laminate where additional reinforcement is needed. This local reinforcement strategy improves the mechanical performance of the component with minimal additional weight and is the focus of the present study.

The optimal placement of such local reinforcement patches is typically computed with evolutionary algorithms, as the problem is non-convex and gradients are not readily available. Mathias et al. [7] represent patches via splines and optimize the shape, orientation, and position of the patch to reinforce a composite structure with a circular hole. The solution shows improved performance over a circular patch, but is limited to a single patch. Zehnder et al. [8] also focus on a single patch, which is represented as a parametric curve in this case. They developed a CAE-pipeline including kinematic draping to map a patch on a curved structure and optimize the global stiffness. Similarly, Fengler et al. [9] perform a multi-objective patch optimization with kinematic draping including experimental validation and Kashfuddoja et al. [10] employ a library of patch for local repair with patches. In contrast to these evolutionary approaches, Schläpfer and Kress [11,12] model patches with *ghost-layers* and compute analytical sensitivities of the objective function w.r.t. to the thickness of these ghost-layers. This enables them to employ a gradient based optimization of eigenfrequencies of panels with cut-outs [11] and optimization of strength of hole-plate specimens including experimental validation [12]. However, their approach is limited to predefined discrete patch orientations of the ghost layers. Particularly relevant for FPP structures are the optimization methods by Rettenwander et al. [13] and Kussmaul et al. [14], as they focus on placing several equal patches. Rettenwander et al. [13] optimize stiffness by deriving continuous fiber paths with an efficient gradient-based approach and employ a multi-linearization method to derive patch positions and orientations. This is corroborated by a concurrent thickness optimization and experimental validation of a sample plate. Kussmaul et al. [14] developed a holistic computational framework for patched laminates. They place patches sequentially accounting for local effects by a shear-lag-submodel [15] as well as kinematic draping.

The objective of this study is to process and optimize locally reinforced FPP structures made from C/C-SiC, as the existing literature focuses on polymer matrix composites only. First, we propose an inverse method to identify the mechanical properties of individual patches from cross-ply laminate tests, as unidirectional layups cannot be tested directly due to limitations of the LSI process. Next, we present a novel, efficient gradient-based optimization method for determining optimal patch locations and orientations utilizing a differentiable finite element solver. This approach allows concurrent optimization of multiple patches (opposed to sequential placement) while directly accounting for manufacturing constraints (opposed to subsequent multi-linearization). This approach is demonstrated on a plate with a central hole, and a two-step curing process is developed to enable the manufacturing of the optimized patched plate. Finally, the optimized design is validated by comparing its stiffness and damage behavior against that of conventional cross-ply laminates.

2. Inverse identification of patch stiffness

C/C-SiC materials typically have a symmetric cross-ply layup to prevent thermal distortion during processing, provide good mechanical properties in various loading directions, and to achieve the desired microstructure with segmentation cracks during processing. Consequently, manufacturing unidirectional C/C-SiC laminates is quite challenging and their properties do not necessarily represent those of a single ply within a cross-ply laminate. Therefore, we need to indirectly infer the anisotropic stiffness parameters $E_{xx}, E_{yy}, G_{xy}, \nu_{xy}$ of individual unidirectional plies from experiments on cross-ply samples.

2.1. Manufacturing of C/C-SiC samples

To determine the material properties, C/C-SiC plates were fabricated by manually stacking twelve layers of phenolic resin-based unidirectional carbon fiber prepreg (SIGRAPREG C U285-0, SGL Carbon SE, Germany) per plate. The fiber volume content of the prepreg in its uncured stage is 46%. Two different laminate configurations were used for tensile testing. The first configuration is a symmetric cross-ply laminate $[0/90/0/90/0/90]_s$, denoted in short form as $[0/90]_{3s}$. The second configuration, also a symmetric cross-ply laminate, followed a $[0/0/90]_{2s}$ stacking sequence, resulting in a higher proportion of fibers oriented in the 0° direction.

After stacking, the laminates were placed between two steel plates and sealed within a vacuum bag. Curing was carried out in an autoclave at 170 °C and 10 bar, with a heating rate of 3.3 K min^{-1} and a dwell time of one hour. After curing, the plates were pyrolyzed up to 900 °C in a nitrogen atmosphere at a heating rate of 1.5 K min^{-1}. Subsequently, the plates were re-infiltrated with phenolic resin Bakelite PF 0433 SW (Bakelite Synthetics, Germany) using an RTM mold. The resin was injected into the mold at 10 bar and cured at 130 °C for 1.5 h. A second pyrolysis step was then performed in a nitrogen atmosphere, reaching 1600 °C, again at a minimum heating rate of 1.5 K min^{-1}. Following the second pyrolysis, the porous carbon structures were infiltrated with molten silicon at 1600 °C under a vacuum of 3 mbar, while continuously purged with Varigon H2 (Linde plc, Germany). Both pyrolysis and silicon infiltration processes were carried out in a high-temperature graphite furnace Tomac+ (Fraunhofer ISC, Germany). The average thickness of the manufactured plates was 3.5 mm, corresponding to an average thickness of 0.3 mm per layer. Test specimens were extracted from the plates using water jet cutting. For tensile testing, tabs made of glass fiber reinforced plastic (GFRP) were bonded with epoxy resin to ensure proper gripping.

2.2. Mechanical characterization of C/C-SiC samples

Tensile tests were performed according to DIN 658-1 using a Zwick Z010 10 kN (Zwick GmbH, Germany) universal testing machine equipped with wedge grips. A 10 N preload was applied and the tests were carried out at a speed of 1.5 mm min^{-1}. For the $[0/0/90]_{2s}$ and $[0/90]_{3s}$ samples, the 0° fiber orientation was aligned with the load direction. Sample displacement was measured using Digital Image Correlation (DIC) with a 12M GOM system (Carl Zeiss AG, Germany). Young's modulus was determined between 2 MPa and 15 MPa using linear regression.

The Iosipescu shear tests were carried out according to ASTM C1292-16 on a Zwick Roell Kappa 050DS 50 kN (Zwick GmbH, Germany) universal testing machine with a preload of 10 N and a speed of 1.5 mm min^{-1}. The $[0/90]_{3s}$ samples were oriented to induce in-plane shear. For the shear tests, the strain measurements were taken from a central area of the specimen that was 1 mm wide and 9 mm high using the same DIC setup as for tensile testing. The shear modulus was calculated in the range from 2 MPa to 15 MPa by linear regression.

Six specimens were tested for both the tensile laminate configurations ($[0/90]_{3s}$ and $[0/0/90]_{2s}$), as well as for the Iosipescu shear tests. Table 1 presents the determined material properties for the two different fiber stackings. Due to signal noise at small displacements, it was not possible to reliably determine the Poisson ratio using DIC. Therefore, the Poisson ratio in the loading directions of 0° and 45° relative to the fiber orientation are taken from Shi et al. [16].

2.3. Evaluation

To compute the anisotropic stiffness of individual patches from cross-ply laminates, we minimize the error between a computed laminate stiffness and the observed laminate stiffness with respect to the properties of an individual patch.

Table 1
Material properties for the two different tested laminates.

Laminate	E_{xx}^{exp}	G_{xy}^{exp}	ν_{xy}^{exp}
$[0/90]_{3s}$	67.69 GPa	8.93 GPa	0.02 [16]
$[\pm 45]_{3s}$	–	–	0.064 [16]
$[0/0/90]_{2s}$	92.06 GPa	–	–

We denote the linear elastic orthotropic material model for a planar stress state

$$\underbrace{\begin{pmatrix}\sigma_{xx}\\ \sigma_{yy}\\ \sigma_{xy}\end{pmatrix}}_{\boldsymbol{\sigma}} = \underbrace{\begin{pmatrix}\frac{E_{xx}}{1-\nu_{xy}\nu_{yx}} & \frac{\nu_{xy}E_{yy}}{1-\nu_{xy}\nu_{yx}} & 0\\ \frac{\nu_{yx}E_{xx}}{1-\nu_{xy}\nu_{yx}} & \frac{E_{yy}}{1-\nu_{xy}\nu_{yx}} & 0\\ 0 & 0 & G_{xy}\end{pmatrix}}_{\mathbf{C}} \underbrace{\begin{pmatrix}\varepsilon_{xx}\\ \varepsilon_{yy}\\ 2\varepsilon_{xy}\end{pmatrix}}_{\boldsymbol{\varepsilon}} \tag{1}$$

with Cauchy stress $\boldsymbol{\sigma}$, orthotropic patch stiffness $\mathbf{C}$, and infinitesimal strain $\boldsymbol{\varepsilon}$. The orthotropic material may be rotated in-plane by an angle ϕ via a rotation operation employing a rotation matrix

$$\mathbf{R}(\phi) = \begin{pmatrix}\cos^2\phi & \sin^2\phi & 2\sin\phi\cos\phi\\ \sin^2\phi & \cos^2\phi & -2\sin\phi\cos\phi\\ -\sin\phi\cos\phi & \sin\phi\cos\phi & \cos^2\phi-\sin^2\phi\end{pmatrix}. \tag{2}$$

Assuming that plies in a laminate of patches with individual rotation angles ϕ_i experience identical strains, we may compute the effective stiffness of a laminate with N layers as

$$\mathbf{C}^{\text{eff}} = \frac{1}{N}\sum_{1}^{N}\mathbf{R}(\phi_i)\mathbf{C}\mathbf{R}^{\top}(\phi_i). \tag{3}$$

The engineering constants of this laminate are then obtained from the corresponding entries of the compliance tensor $\mathbf{S}^{\text{eff}} = \mathbf{C}^{\text{eff}-1}$ as

$$E_{xx}^{\text{eff}} = \frac{1}{S_{11}^{\text{eff}}} \quad , \quad E_{yy}^{\text{eff}} = \frac{1}{S_{22}^{\text{eff}}} \quad , \quad G_{xy}^{\text{eff}} = \frac{1}{S_{33}^{\text{eff}}} \quad \text{and} \quad \nu_{xy}^{\text{eff}} = -\frac{S_{12}^{\text{eff}}}{S_{22}^{\text{eff}}}. \tag{4}$$

Now, we seek the set of patch parameters $E_{xx}, E_{yy}, G_{xy}, \nu_{xy}$ that minimizes the relative error between effective laminate properties and observed experimental stiffnesses for the corresponding laminates. The objective function is formulated as relative root mean squared error

$$\begin{aligned} e(E_{xx}, E_{yy}, G_{xy}, \nu_{xy}) = \frac{1}{5}\Bigg[&\left(\frac{E_{xx}^{\text{eff, }[0/90]} - E_{xx}^{\text{exp, }[0/90]}}{E_{xx}^{\text{exp, }[0/90]}}\right)^2 \\ &+ \left(\frac{G_{xy}^{\text{eff, }[0/90]} - G_{xy}^{\text{exp, }[0/90]}}{G_{xy}^{\text{exp, }[0/90]}}\right)^2 \\ &+ \left(\frac{E_{xx}^{\text{eff, }[0/0/90]} - E_{xx}^{\text{exp, }[0/0/90]}}{E_{xx}^{\text{exp, }[0/0/90]}}\right)^2 + \left(\frac{\nu_{xy}^{\text{eff, }[0/90]} - \nu_{xy}^{\text{exp, }[0/90]}}{\nu_{xy}^{\text{exp, }[0/90]}}\right)^2 \\ &+ \left(\frac{\nu_{xy}^{\text{eff, }[\pm 45]} - \nu_{xy}^{\text{exp, }[\pm 45]}}{\nu_{xy}^{\text{exp, }[\pm 45]}}\right)^2\Bigg]^{\frac{1}{2}}, \end{aligned} \tag{5}$$

where the effective elastic properties are evaluated according to Eqs. (3) and (4) as functions of $E_{xx}, E_{yy}, G_{xy}, \nu_{xy}$. The optimization problem

$$\begin{aligned} \min_{E_{xx},E_{yy},G_{xy},\nu_{xy}} \quad & e(E_{xx}, E_{yy}, G_{xy}, \nu_{xy}) \\ \text{s.t.} \quad & 1\,\text{GPa} < E_{xx} < 400\,\text{GPa} \\ & 0.1\,\text{GPa} < E_{yy} < 200\,\text{GPa} \\ & 0.1\,\text{GPa} < G_{xy} < 300\,\text{GPa} \\ & -10 < \nu_{xy} < 10 \end{aligned} \tag{6}$$

is then solved with a differential evolution algorithm in SciPy [17,18] with a tolerance of 10^{-10}.

Table 2
Orthotropic elastic properties of a single patch.

E_{xx}	E_{yy}	G_{xy}	ν_{xy}
136.10 GPa	1.44 GPa	8.69 GPa	0.954

2.4. Results and discussion

The minimization leads to a final relative root mean squared error of 1.3% for the patch parameters listed in Table 2. These parameters lead to the orientation dependent engineering constants illustrated with polar plots in Fig. 1 for different load cases. The black points indicate the measured properties in the respective direction. They highlight a good agreement between effective parameters computed from the patch parameters and observed stiffnesses.

The proper choice of experimental setups, especially including an unbalanced $[0/0/90]_{2s}$ cross ply setup, provides a strong indication that the solution to the optimization problem appears well posed with a unique solution. This is supported by the observation that the differential evolution algorithm consistently results in the same set of parameters regardless of the initial random sampling. However, the weighting of relative errors influences the outcome slightly. Weighting each error equally seems a natural choice, but might be adjusted to put more emphasis on specific elastic constants.

3. Gradient-based patch optimization

As a test case, we consider a plate with an elliptical hole, as depicted in Fig. 2. The plate is subjected to uniaxial tension in the vertical direction, with clamped regions at top and bottom. The base plate is fabricated from a $[0/90]_{2s}$ cross-ply base-layup and additional reinforcement patches, which should be placed on both sides of the plates for symmetry. The objective is to optimize the placement and orientation of the reinforcement patches to maximize the overall stiffness of the structure. The patch size is fixed at 30 mm by 10 mm, representing a compromise between manufacturing feasibility and geometric fidelity.

In this design, the elliptical hole interrupts the momentum flux through the plate. This causes stress concentrations and poses a challenging problem for finding optimal reinforcement patch configurations. Due to symmetry, it is sufficient to model only a quarter of the plate, which is indicated in dark gray in Fig. 2.

3.1. Methodology

We describe a patch configuration of N patches by tuples $\{x_p, y_p, \theta_p\}$, where the tuple summarizes the location and orientation of each patch. For each patch, we create two *ghost patches* mirrored along the x-axis and y-axis, respectively. These ghost patches account for symmetry in the patch configuration by ensuring that any patch crossing a symmetry plane is accurately contributing to the stiffness (see Fig. 4(a) for an example). Hence, there are N independent tuples, but $p \in [1, 3N]$ due to the ghost patches.

Given a patch configuration, we want to determine the stiffness of the test geometry and the gradient of the stiffness w.r.t. to the patch configuration for subsequent optimization. Hence, the computational domain is meshed with second order 6-node triangle elements and patches are projected in a smooth manner onto the elements using Gaussian weights

$$w_p = e^{-\epsilon^2\left(\hat{\xi}_p^2 + \hat{\eta}_p^2\right)} \tag{7}$$

with

$$\hat{\xi}_p = \max\left(0, |\xi_p| - \frac{L}{2} + \frac{\sqrt{\ln 2}}{\epsilon}\right) \tag{8}$$

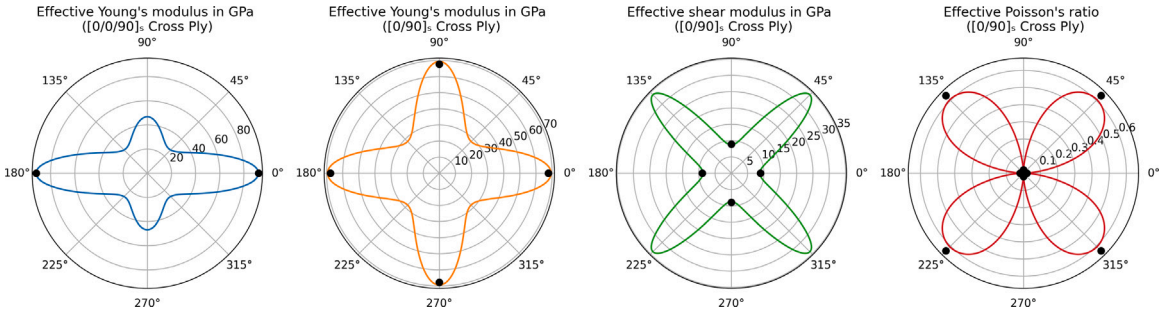

Fig. 1. Polar plots comparing effective stiffness computed from single patch properties (see Table 2) with the observed experimental data for different experimental setups.

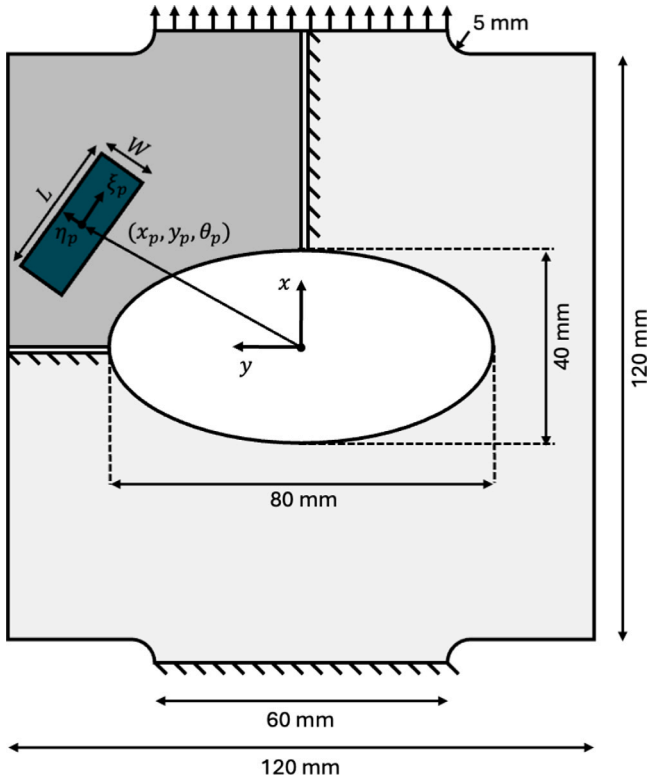

Fig. 2. Test geometry with dimensions and load case. The position of each patch is described via a tuple (x_p, y_p, θ_p) denoting the two coordinates of the patch's center and its orientation angle, respectively.

$$\hat{\eta}_p = \max\left(0, |\eta_p| - \frac{W}{2} + \frac{\sqrt{\ln 2}}{\epsilon}\right), \tag{9}$$

where ξ_p and η_p describe locations in a local patch coordinate system (see Fig. 2). The weighting smooths the reinforcing effect of patches, assigning $w_p = 1$ within a patch, $w_p = 0.5$ at the edge of the patch and gradually reducing to $w_p \to 0$ outside the patch, as illustrated in Fig. 3 for a slice across a patch with $W = 10\,\text{mm}$ The Gaussian weighting ensures that integrating the patch weight over the entire domain equals the patches surface area. The parameter ϵ controls the smoothing region and is set to $\epsilon = 0.5$ in this work.

Fig. 4 illustrates the projection of three exemplary patches to the quarter plate via the smoothed weighting approach. In the example, one patch crosses a symmetric boundary, which is accounted for by the weights of its ghost patch.

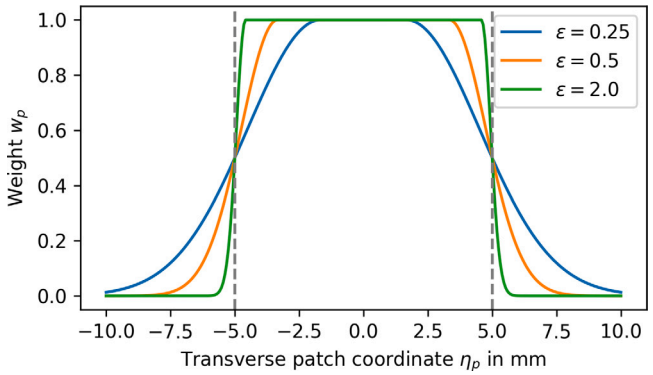

Fig. 3. Exemplary weight distribution across a patch with $W = 10\,\text{mm}$ for different choices of ϵ.

After the projection, the local thickness of the plate is computed from the $[(0/90)_{2s}]$ base layup and the contributions from reinforcement patches according to

$$\tilde{t} = 8t_0 + 2t \sum_{p=1}^{3N} w_p \tag{10}$$

with a thickness t_0 =0.3 mm for each layer in the base layup and t =0.2 mm average thickness in the patches. The reinforcement patches are compressed more during the two-step curing process (see Sections 4.1 and 4.2) and are thus assumed to be thinner on average. The stiffness is computed as

$$\tilde{\mathbf{C}} = \frac{1}{\tilde{t}}\left(8t_0\mathbf{C}^0 + 2t\sum_{p=1}^{3N} w_p\mathbf{C}_p\right) \tag{11}$$

with the effective stiffness of the base layup $\mathbf{C}^0$ and the stiffness of a patch $\mathbf{C}_p$, which accounts for rotation.

With the thickness and stiffness assigned, we employ the differentiable Finite Element solver TORCH-FEM[1] to compute the nodal displacements u_i and forces f_i. This enables the evaluation of the strain energy, defined as $W = \frac{1}{2}\sum_i u_i f_i$, which serves as a measure of the global average stiffness of the part. Based on this, the optimization problem is formulated as

$$\max_{\{x_p, y_p, \theta_p\}_{p=1}^{N}} \frac{W}{W^0} + \lambda\frac{V}{V^0}, \tag{12}$$

where W^0 is the strain energy of the base plate, and V and V_0 represent the total volume of the patched plate and base plate, respectively.

[1] https://github.com/meyer-nils/torch-fem.

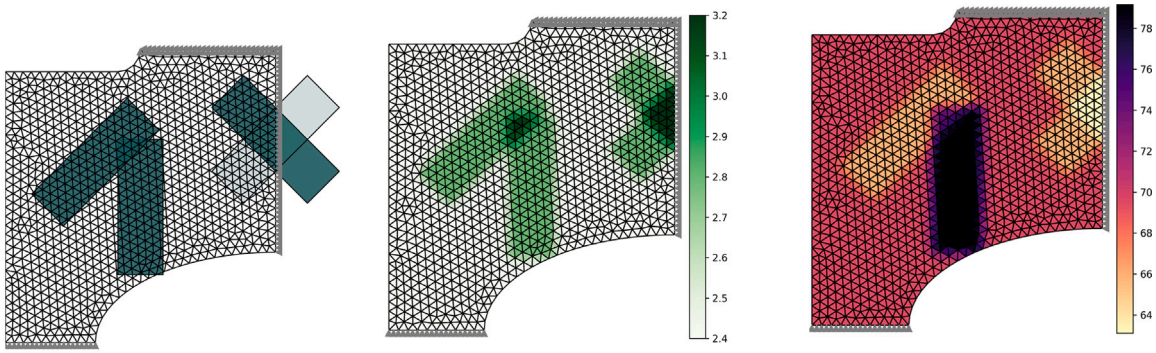

(a) Exemplary patch configuration. (b) Thickness $\tilde{t}$ in mm. (c) Stiffness component $\tilde{C}_{xx}$ in GPa.

Fig. 4. Illustration of the weights for an exemplary patch configuration of three patches on a symmetric quarter model of the plate. One patch crosses a symmetric boundary demonstrating the effect of weighting a *ghost-patch*, which is shown with reduced opacity in (a).

The second term acts as a regularization term to penalize patches placed outside the desired geometry, with the penalty factor λ linearly ramped from 0.0 to 100.0 during the optimization process. The optimization problem is solved using a gradient decent approach (ADAM with learning rate 0.1 and 1000 iterations) using PyTorch's automatic differentiation. Given the non-convex nature of the problem and the potential for multiple local optima, we perform at least ten independent optimizations, each starting from a different random patch configuration generated via Latin Hypercube Sampling, and report the best results.

3.2. Results and discussion

The unreinforced base plate consisting of a $[0/90]_{2s}$ cross-ply layup features a component stiffness of $23.69\,\mathrm{kN\,mm^{-1}}$. The normalized first principal stress σ_I/σ_0, with the nominal stress at the clamping σ_0, is illustrated in Fig. 5. It shows stress concentrations near the clamping and the ellipse's vertices, with a maximum stress concentration factor of 6.53 near the elliptical hole.

Adding a single patch ($N = 1$) to the quarter plate – corresponding to a total of eight patches due to symmetries – increases the overall stiffness by 16%, while the weight increases only by 1.6%. This makes the local reinforcement significantly more effective than the base laminate. The best result obtained via multi-start gradient descent optimization is shown in Fig. 6(a). In this configuration, the patches primarily reinforce the regions near the clamps.

For $N = 2$ (16 patches in total), the best solution places patches at the two regions with highest stress concentration: near the clamps and at the ellipse's vertices (see Fig. 6(b)). This configuration is robust, as it is reached for many restarts with different random initial conditions. The resulting stiffness is improved by 24%, with a corresponding weight increase of only 3.3%.

For $N = 4$ (32 patches in total), the configuration shown in Fig. 6(c) increases stiffness by 48%, while the weight increases by 6.5%. The solution closely resembles the $N = 2$ case, but with three patches stacked near the clamping region.

For $N = 8$ (64 patches in total), several local optima with comparable performance but reduced robustness emerge. One of the best solutions, depicted in Fig. 6(d), achieves a 65% increase in stiffness at the cost of a 13% increase in weight. Although still more efficient than the base laminate, the stiffness-to-weight gain is lower than in the cases with fewer patches.

All solutions tend to prioritize reinforcing the clamping regions over the stress concentration zones near the elliptical hole, despite higher stress at the hole. This is because the clamped areas appear four times in the symmetric geometry, while the hole-related stress concentrations occur only twice. Consequently, more patches are required to reinforce the clamps. In contrast, a single patch at the hole adds two layers of reinforcement in the critical region due to symmetry, making it a more efficient reinforcement. In addition, patches placed at the hole are able to redirect the stress away from the hole, while stress concentrations near the clamping cannot be avoided. Hence, patches are most efficient close to the clamped region.

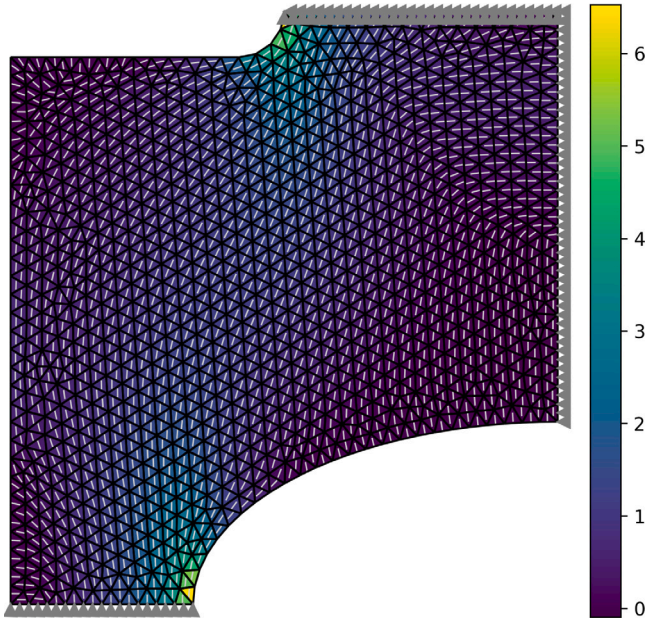

Fig. 5. Normalized first principal stress of the non-reinforced base plate ($N = 0$, $23.69\,\mathrm{kN\,mm^{-1}}$, Volume: $30\,020\,\mathrm{mm^3}$). Light gray lines indicate the direction of the first principal stress. Note: For better visibility of these directions, the reader is encouraged to consult the high-resolution electronic version of the manuscript and utilize the zoom function.

The optimization problem is non-convex, so a multi-start strategy is employed to identify optimal solutions. Leveraging automatic differentiation in TORCH-FEM, the gradient-based optimizer achieves approximately six iterations per second on an Apple M1 chip — orders of magnitude faster than a comparable genetic algorithm implemented in PyGAD.

4. Validation

To demonstrate the effect of optimized local C/C-SiC patch reinforcements, the solution depicted in Fig. 6(d) was manufactured, analyzed and tested. To the authors' knowledge, this represents the first demonstration of an optimized, locally patched C/C-SiC component with variable thickness.

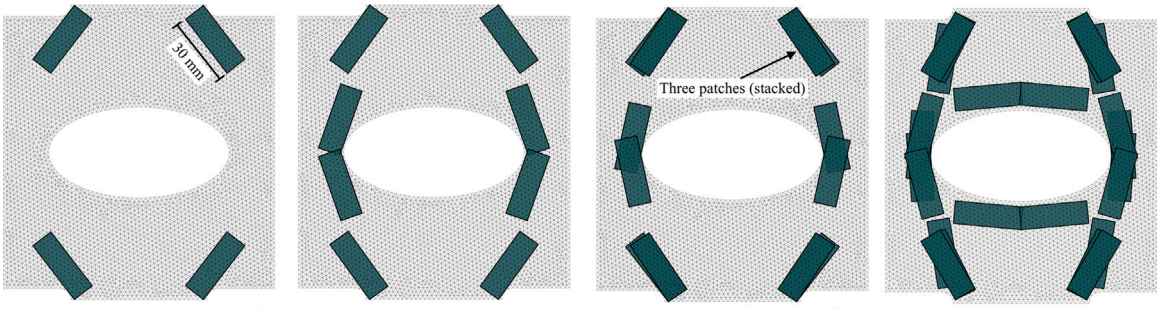

Fig. 6. Optimal patch configurations for patches with dimensions 30 mm by 10 mm.

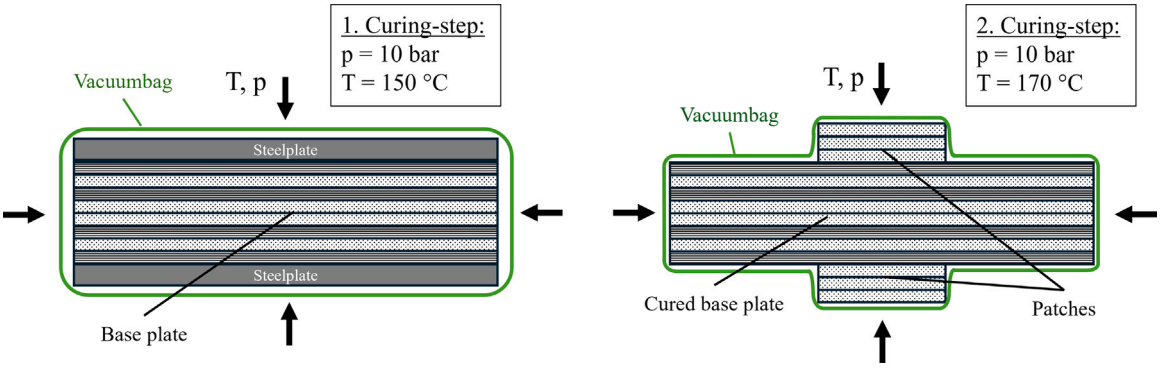

Fig. 7. Schematic overview of the two-step curing process.

4.1. Manufacturing of C/C-SiC samples

To manufacture the base plates, eight layers of the carbon fiber prepreg were manually stacked to form a symmetrical cross-ply laminate with fiber orientations at 0° and 90°. After stacking, the laminate was placed between two steel plates and sealed within a vacuum bag. The curing process was carried out in an autoclave, with a temperature of 150 °C and an overpressure of 10 bar. The heating rate was set at 3.3 K min^{-1}, and the dwell time was one hour. In the manufacturing of patched plates, uncured prepreg patches (30 mm × 10 mm) were applied onto cured CFRP base plates on both sides using a template according to the optimized pattern. These patched plates were sealed within a vacuum bag again, this time without additional steel plates. Curing of the patches occurred at an elevated temperature of 170 °C, maintaining the same overpressure, heating rate and dwell time as used for the base plates. Further steps involving pyrolysis, reinfiltration, and siliconization followed the methods described in Section 2.1. The final geometry of the samples was obtained through wire erosion. A schematic overview of the two-step curing process is shown in Fig. 7.

4.2. Morphology of C/C-SiC samples

Fig. 8 shows a patched CFRP plate (after second curing) and a siliconized patched C/C-SiC plate. After curing, the patch structures are clearly visible on the surface. Since no steel plates were used during the second curing step, the vacuum foil could conform closely to the patches, preserving the intended structure. The fine surface structure of the CFRP plate comes from the use of vacuum fleece and disappears following the first pyrolysis. After siliconization, the patch structure remains intact. The surface exhibits the typical gray to silvery color characteristic of C/C-SiC, which results from a combination of pure silicon and SiC. The small droplets observed on the surface are attributed to the density anomaly of silicon [19], since the silicon undergoes a volume expansion upon solidification, pressing the silicon out of the plate.

Fig. 9 shows a cross-section at the location with 18 layers, captured using a light microscope. In this image, the patches protrude vertically from the image plane, revealing the characteristic microstructure of C/C-SiC with distinct phases. These phases consist of carbon fibers embedded within an amorphous carbon matrix (light gray color), characterized by a discrete block structure. These blocks are separated by segmentation cracks filled with free silicon (white color). At the interface between silicon and carbon, a SiC layer (dark gray color) has formed. Black regions within the blocks represent pores that were either too small to allow silicon infiltration or closed pores [20–22]. Black translaminar cracks are visible, resulting from thermal expansion mismatch coefficients between the phases during cooling [23,24].

The eight layers for the base plate are clearly identifiable. Despite the 0°/90° laminate being only present in the base plate, segmentation cracks are visible in all layers attributed to the angled sectioning of the specimen.

Due to the similar fiber orientation in the patches distinguishing between layers is not possible. No delaminations between base plate and patches are visible, and layers remain firmly bonded by the carbon matrix. Segmentation cracks in the patched layers are translaminar suggesting strong adhesion during pyrolysis. The shrinkage of the patched layers was restricted by the base plate and internal stresses in the matrix were relieved through segmentation cracking [5].

During processing, the patches lose their original straight shape and instead adopt a more rounded form. This phenomenon could be attributed to two factors. Firstly, the vacuum bagging film does not completely replicate the rectangular shape of the patches. Secondly, phenolic resin exhibits low viscosity at elevated temperatures prior to curing [25]. This reduced viscosity significantly facilitates fiber movement under increased pressure during the curing process.

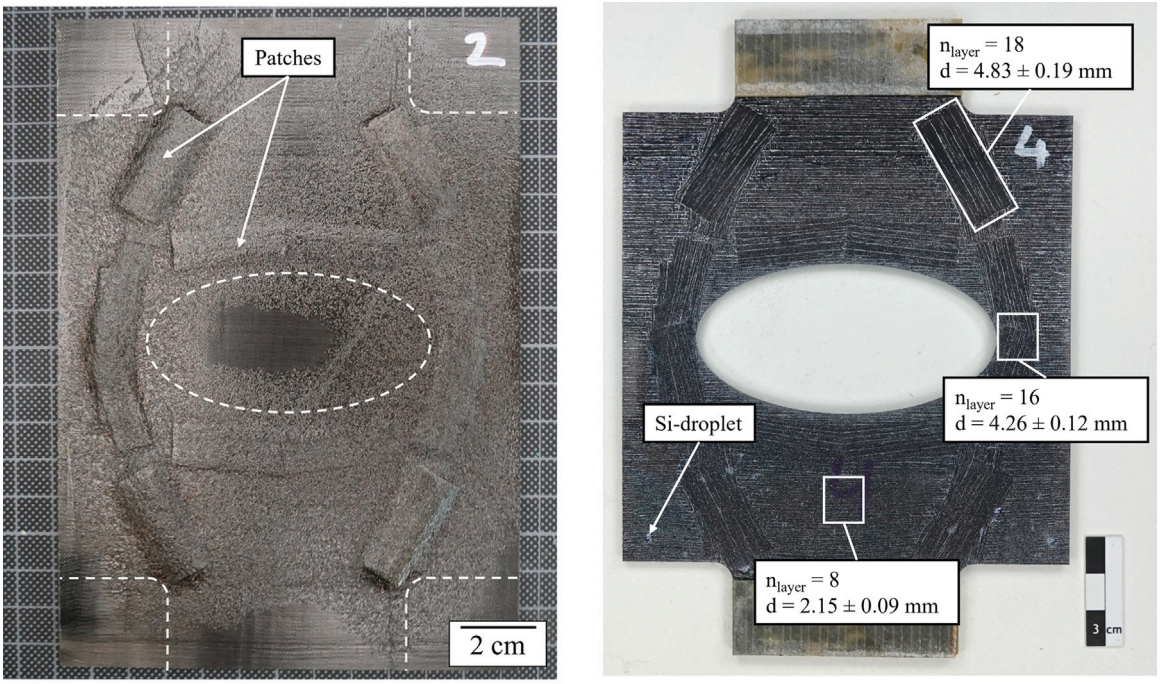

(a) (b)

Fig. 8. Picture of the (a) patched CFRP plate after curing the patches and the (b) patched C/C-SiC sample after siliconization. The number of layers and their respective thicknesses with standard deviation in the ellipse and clamping areas are also shown.

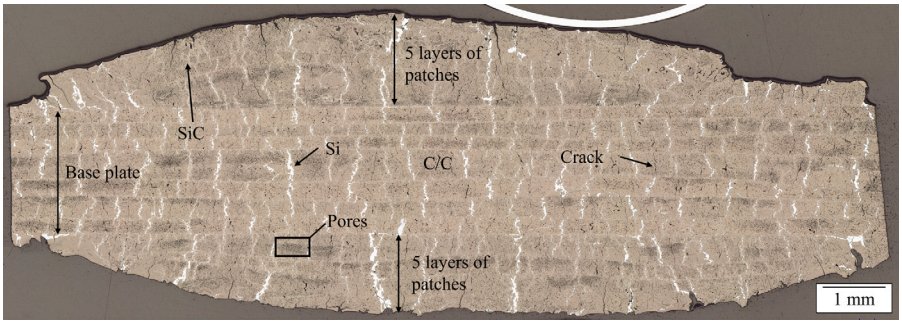

Fig. 9. Light microscopy image of a cross-section of C/C-SiC with 18 layers. The patches are oriented perpendicular to the image plane.

The base plate exhibits an average thickness of 2.15 mm. In the patched regions, a thickness of 4.83 mm was measured near the clamping area for 18 layers and 4.26 mm near the elliptical region for 16 layers. This corresponds to an average layer thickness of approximately 0.27 mm for both the patches and the base plate. However, the thickness measurements were taken at the locations of maximum height. Due to the rounded surface geometry, the actual average thickness is therefore expected to be slightly lower. Compared with the plates manufactured for the determination of elastic properties, the center-holed plates show a reduction in thickness during the manufacturing process. This effect may be attributed to resin loss during processing. It is assumed that the absolute amount of resin lost during manufacturing remains approximately constant. Consequently, this loss has a more pronounced effect when fewer layers are present, resulting in a higher fiber volume fraction and thinner individual layers.

4.3. Mechanical characterization of center-holed C/C-SiC samples

Mechanical characterization of the center-holed plates was conducted through cyclic tensile testing using a Zwick Roell Kappa 050DS 50 kN universal testing machine. Samples were clamped using wedge grips. The testing procedure began with an initial load of 400 N, which was increased incrementally by 400 N after each cycle until the sample failed. A preload of 50 N was applied, and specimens were unloaded to this level after each cycle. The loading and unloading speed was set to 2 mm min^{-1} up to a load of 2000 N and then increased to 4 mm min^{-1}. Sample displacement was measured via Digital Image Correlation (DIC) using a 12M GOM system. The average displacement from three virtual extensometers was used to determine the total displacement. Component stiffness was calculated using linear regression between 50 N and 1200 N for each cycle. In total, two reference (unpatched) plates and three patched plates were tested.

After each cycle, both component stiffness K and permanent displacement u_0 were evaluated. Fig. 10(a) shows the evolution of component stiffness across the load cycles. Due to settling effects, stiffness evaluation began from the third cycle (1200 N). The patched plates exhibited an average component stiffness of 38.8 ± 0.2 kN mm^{-1}. Variations between individual cycles are attributed to signal noise at small displacements. By cycle 13 (5200 N), stiffness had decreased to an average of 35.4 ± 1.2 kN mm^{-1}, corresponding to a 9% reduction. In contrast, the initial stiffness of the unpatched plates was significantly

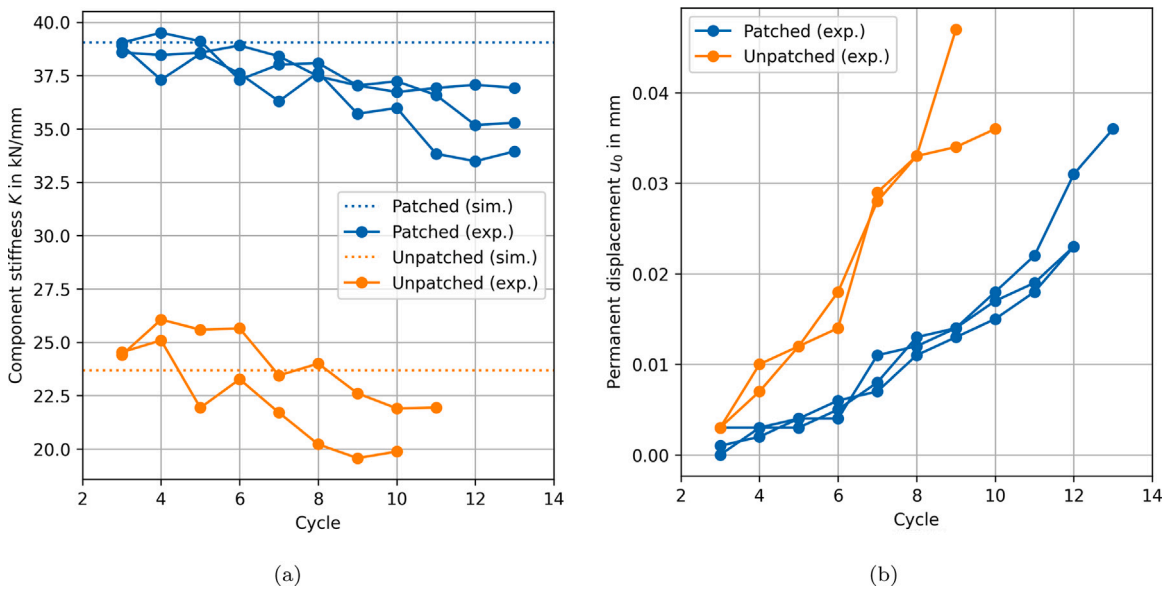

Fig. 10. (a) Component stiffness and (b) permanent displacement over load cycles for unpatched and patched center-holed C/C-SiC samples.

lower at 24.5 kN mm^{-1}, decreasing to 20.9 ± 1.1 kN mm^{-1} by cycle 13, which corresponds to a 14% reduction.

Patch optimization resulted in an improvement in initial stiffness by approximately 58%, achieved with only a with a weight increase of 14%. This demonstrates good agreement with simulation results, as indicated by the dashed line in Fig. 10(a). Due to high processing complexity, only a limited number of specimens could be tested. Nevertheless, the experimental data clearly indicate a consistent trend.

Fig. 10(b) illustrates the evolution of u_0 over the load cycles. Permanent displacement u_0 was evaluated after each cycle up to cycle 12. At the third cycle, the patched samples show negligible permanent displacement, which gradually increases in subsequent cycles. All patched samples exhibit similar trends, reaching 0.025 ± 0.004 by cycle 12. In comparison, unpatched samples show a notably steeper increase with the cycles. Prior to failure, occurring between cycles 9 and 10, the u_0 values for unpatched samples range between 0.036 mm and 0.047 mm.

Both patched and unpatched plates exhibited typical damage behavior of CMC materials under cyclic loading [26,27]. In CMCs, cracks typically initiate in the matrix due to its lower fracture strain compared to the fibers. These matrix cracks propagate toward the fibers and are deflected at the fiber–matrix interface, provided the interfacial fracture toughness is sufficiently low [28]. As the loading increases, the matrix crack density grows, reducing the effective cross-sectional area and thus decreasing component stiffness. A slight reduction in stiffness can be observed even after a few loading cycles. The increase in u_0 can be largely attributed to friction and sliding effects in fractured regions. As matrix cracks open during loading, part of the displacement is not recovered during unloading. With continued cyclic loading, more cracks develop, and this effect becomes increasingly significant.

Fig. 11 shows the uniaxial strain field (ε_{yy}) obtained from DIC measurements for the unpatched and patched plates at 3600 N. For the unpatched plate, increased strain concentrations (indicated by red areas) are observed in the ellipse region, as well as in the notched area near the clamping. In both regions, a change in cross-section occurs, which leads to local increases in strain. For the patched plate, slight strain increases are also observed around the elliptical area. The highest strains are found between two patch clusters, where no patches are present in the pattern, and in the notched area near the clamping. In these regions, the change in cross-section also results in local strain concentrations. Between the two patch clusters, the change in cross-section occurs in the thickness direction. Overall, the unpatched plates exhibit significantly higher strains under the same load compared to the patched plates.

Table 3
Overview of the force at break, the specific force at break, the initial stiffness and the specific initial stiffness.

Type	Force at break	Specific force at break	Initial stiffness	Specific initial stiffness
Patched	6063 N	68 N g^{-1}	38.8 kN mm^{-1}	0.44 kN mm^{-1} g^{-1}
Unpatched	3410 N	44 N g^{-1}	24.5 kN mm^{-1}	0.31 kN mm^{-1} g^{-1}

Table 3 summarizes the average force at break, specific force at break, initial stiffness, and specific initial stiffness with standard deviation for the center-holed C/C–SiC samples. Both unpatched plates fractured in the elliptical region, while all patched plates failed in the clamping area. The patched plates exhibited an average force at break of 6063 ± 598 N, significantly higher than that of unpatched plates, which failed at 3410 ± 215 N. Comparing the specific force at break, the patched plates demonstrated a 55% increase.

The localized application of patches not only increased component stiffness but also significantly enhanced the force at break. Patching led to substantial local thickening, with more than a doubling of thickness in critical areas. This thickening contributed to the reduction of u_0, indicating fewer matrix cracks under equivalent loading conditions. This assumption is supported by the strain field results. Reduced matrix cracking improves load transfer between fibers and matrix, decreasing the likelihood of local fiber overloading in the vicinity of cracks [29]. Consequently, this lowers the probability of premature fiber failure. Ultimately, this contributes to a higher force at break in patched plates, with failure occurring in the clamping region. Since this region cannot be reinforced with patches, it remains the structural weak point.

5. Conclusion

This work presents methods for parameter identification, structural optimization, and processing for ceramic matrix composites manufactured with the fiber patch placement process. As a validation example, a locally reinforced, center-holed C/C-SiC plate was optimized, manufactured and experimentally tested. The conclusion are summarized as follows:

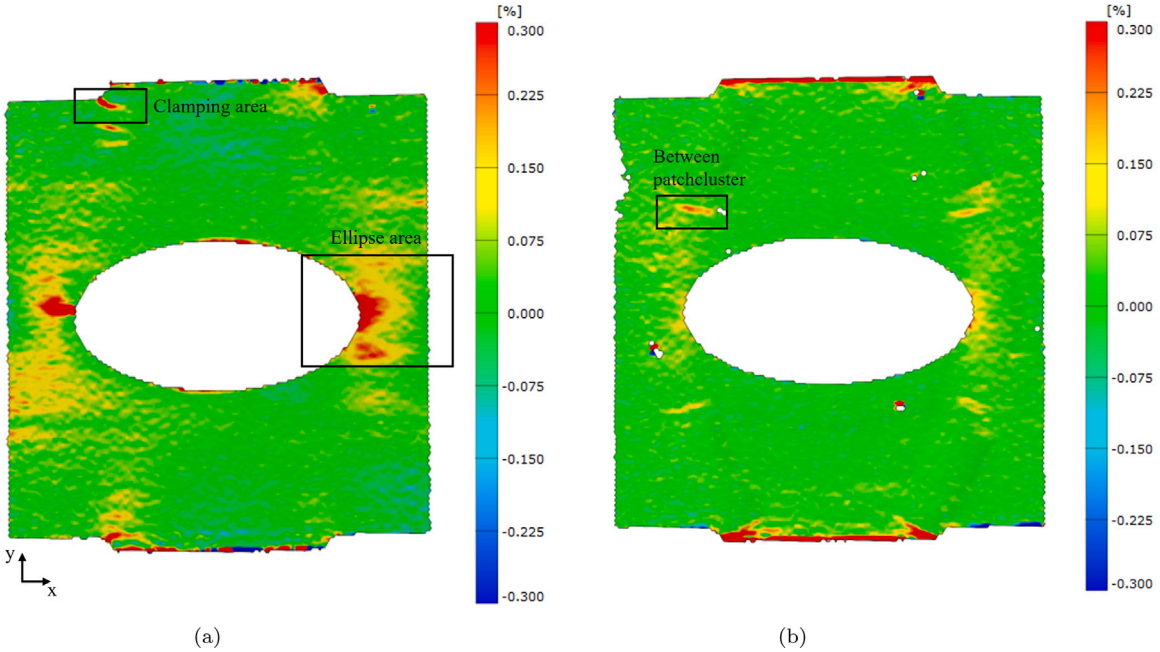

Fig. 11. Uniaxial strain field (ε_{yy}) of the (a) unpatched plate and (b) patched plate at 3600 N.

- The inverse parameter identification method enables the determination of single layer orthotropic elastic patch properties with an error of 1.3% even though the manufacturing is restricted to cross-ply laminates. The proper choice of experimental setups, especially including a unbalanced $[0/0/90]_{2s}$ cross ply setup, provides strong indication that the solution to the optimization problem is well posed.
- Gradient-based optimization of patch positions via a smoothed patch projection and a differentiable FEM solver increases the stiffness efficiently. The optimization accounts for hard constraints on symmetry and soft constraints on the domain.
- By sequentially curing the patched CFRP preform, the desired structure could be successfully realized using the LSI process. Microscopic analysis shows excellent adhesion between the reinforcement patches and the base plate.
- Cyclically increasing tensile tests demonstrate good agreement between experimental results (component stiffness: $38.8\,\mathrm{kN\,mm^{-1}}$) and numerical simulations (initial component stiffness: $39.05\,\mathrm{kN\,mm^{-1}}$). The use of patches increased initial stiffness by 59% with a weight increase of only 14%. In addition to increased stiffness, an enhancement of strength was observed, mainly attributed to the more than doubling of thickness in critical areas. Local reinforcement causes a shift in the failure location from the region of the ellipse to the clamping area. Given the significant manufacturing complexity, the experimental campaign was necessarily restricted to small sample sizes. Although the results show consistent trends and strong agreement with simulations, these findings should be interpreted within the context of their inherent statistical limitations.

The methods presented in this work for processing and optimizing locally patched C/C-SiC structures have shown promising results. The approaches appear to be suitable for both optimization and practical implementation. As a possible next step, future investigations could focus on optimizing not only for stiffness but also for strength. Additionally, following the successful demonstration on two-dimensional structures, it may be worthwhile to consider fully patched components with more complex geometries, both in two and three dimensions.

CRediT authorship contribution statement

Jonas Riesner: Writing – original draft, Visualization, Methodology. **Dietmar Koch:** Writing – review & editing, Conceptualization. **Nils Meyer:** Writing – original draft, Software, Conceptualization.

Declaration of competing interest

The authors declare that they have no known competing financial interests or personal relationships that could have appeared to influence the work reported in this paper.

Acknowledgments

The research documented in this manuscript has been supported by the Hightech Agenda Bavaria, Germany. The support by the Bavarian State Government, Germany is gratefully acknowledged. The authors acknowledge the financial support from the Deutsche Forschungsgemeinschaft, Germany (DFG funding/Project number 454647179) for funding the high temperature graphite analytical furnace used in this study.

Data availability

The patch optimization code is available as Jupyter Notebook in the TORCH-FEM GitHub repository in the *examples/optimization/planar* directory.

References

[1] Heidenreich B. C/SiC and C/C–SiC composites. In: Bansal NP, Lamon J, editors. Ceramic matrix composites: Materials, modeling and technology. Wiley-VCH; 2015, p. 147–216. http://dx.doi.org/10.1002/9781118832998.ch6.
[2] Heidenreich B. Melt infiltration process. In: Krenkel W, editor. Ceramic matrix composites: Fiber reinforced ceramics and their applications. Wiley-VCH; 2008, p. 113–39. http://dx.doi.org/10.1002/9783527622412.ch5.
[3] Launey ME, Ritchie RO. On the fracture toughness of advanced materials. Adv Mater 2009;21(20):2103–10. http://dx.doi.org/10.1002/adma.200803322.
[4] Ko T-H, Kuo W-S, Chang Y-H. Microstructural changes of phenolic resin during pyrolysis. J Appl Polym Sci 2001;81(5):1084–9. http://dx.doi.org/10.1002/app.1530.

[5] Schulte-Fischedick J, Seiz S, Lützenburger N, Wanner A, Voggenreiter H. The crack development on the micro- and mesoscopic scale during the pyrolysis of carbon fibre reinforced plastics to carbon/carbon composites. Compos Part A: Appl Sci Manuf 2007;38(10):2171–81. http://dx.doi.org/10.1016/j.compositesa.2007.06.013.

[6] Bianchi I, Forcellese A, Simoncini M, Vita A, Delledonne L, Castorani V. Life cycle assessment of carbon ceramic matrix composite brake discs containing reclaimed prepreg scraps. J Clean Prod 2023;413:137–537. http://dx.doi.org/10.1016/j.jclepro.2023.137537.

[7] Mathias J-D, Balandraud X, Grediac M. Applying a genetic algorithm to the optimization of composite patches. Comput Struct 2006;84(12):823–34. http://dx.doi.org/10.1016/j.compstruc.2005.12.004.

[8] Zehnder N, Ermanni P. Optimizing the shape and placement of patches of reinforcement fibers. Compos Struct 2007;77(1):1–9. http://dx.doi.org/10.1016/j.compstruct.2005.05.011.

[9] Fengler B, Schäferling M, Schäfer B, Bretz L, Lanza G, Häfner B, Hrymak A, Kärger L. Manufacturing uncertainties and resulting robustness of optimized patch positions on continuous-discontinuous fiber reinforced polymer structures. Compos Struct 2019;213:47–57. http://dx.doi.org/10.1016/j.compstruct.2019.01.063.

[10] Kashfuddoja M, Ramji M. Design of optimum patch shape and size for bonded repair on damaged Carbon fibre reinforced polymer panels. Mater Des (1980-2015) 2014;54:174–83. http://dx.doi.org/10.1016/j.matdes.2013.08.043.

[11] Schläpfer B, Kress G. A sensitivity-based parameterization concept for the automated design and placement of reinforcement doublers. Compos Struct 2012;94(3):896–903. http://dx.doi.org/10.1016/j.compstruct.2011.08.034.

[12] Schläpfer B, Kress G. Optimal design and testing of laminated light-weight composite structures with local reinforcements considering strength constraints part I: Design. Compos Part A: Appl Sci Manuf 2014;61:268–78. http://dx.doi.org/10.1016/j.compositesa.2014.02.008.

[13] Rettenwander T, Fischlschweiger M, Machado M, Steinbichler G, Major Z. Tailored patch placement on a base load carrying laminate: A computational structural optimisation with experimental validation. Compos Struct 2014;116:48–54. http://dx.doi.org/10.1016/j.compstruct.2014.04.028.

[14] Kussmaul R, Jónasson JG, Zogg M, Ermanni P. A novel computational framework for structural optimization with patched laminates. Struct Multidiscip Optim 2019;60:2073–91. http://dx.doi.org/10.1007/s00158-019-02311-w.

[15] Kussmaul R, Zogg M, Ermanni P. An efficient two-dimensional shear-lag model for the analysis of patched laminates. Compos Struct 2018;206:288–300. http://dx.doi.org/10.1016/j.compstruct.2018.07.093.

[16] Shi Y, Li S, Sitnikova E, Cepli D, Koch D. Experimental evaluation and theoretical prediction of elastic properties and failure of C/C–SiC composite. Int J Appl Ceram Technol 2022;19(1):7–21. http://dx.doi.org/10.1111/ijac.13775.

[17] Virtanen P, Gommers R, Oliphant TE, Haberland M, Reddy T, Cournapeau D, Burovski E, Peterson P, Weckesser W, Bright J, van der Walt SJ, Brett M, Wilson J, Millman KJ, Mayorov N, Nelson ARJ, Jones E, Kern R, Larson E, Carey CJ, Polat İ, Feng Y, Moore EW, VanderPlas J, Laxalde D, Perktold J, Cimrman R, Henriksen I, Quintero EA, Harris CR, Archibald AM, Ribeiro AH, Pedregosa F, van Mulbregt P, SciPy 10 Contributors. SciPy 1.0: Fundamental algorithms for scientific computing in python. Nature Methods 2020;17:261–72. http://dx.doi.org/10.1038/s41592-019-0686-2.

[18] Storn R, Price K. Differential evolution – A simple and efficient heuristic for global optimization over continuous spaces. J Global Optim 1997;11(4):341–59. http://dx.doi.org/10.1023/A:1008202821328.

[19] Kimura S, Terashima K. A review of measurement of thermophysical properties of silicon melt. J Cryst Growth 1997;180(3–4):323–33. http://dx.doi.org/10.1016/S0022-0248(97)00263-7.

[20] Wang Y, Tan S, Jiang D. The effect of porous carbon preform and the infiltration process on the properties of reaction-formed SiC. Carbon 2004;42(8–9):1833–9. http://dx.doi.org/10.1016/j.carbon.2004.03.018.

[21] Zhao Y, Xia H, Tang R, Shi Z, Yang J, Wang J. A low cost preparation of C/SiC composites by infiltrating molten Si into gelcasted pure porous carbon preform. Ceram Int 2015;41(5):6478–87. http://dx.doi.org/10.1016/j.ceramint.2015.01.087.

[22] Xu S, Qiao G, Li D, Yang H, Liu Y, Lu T. Reaction forming of silicon carbide ceramic using phenolic resin derived porous carbon preform. J Eur Ceram Soc 2009;29(11):2395–402. http://dx.doi.org/10.1016/j.jeurceramsoc.2009.01.022.

[23] Breede F, Koch D, Maillet E, Morscher GN. Modal acoustic emission of damage accumulation in C/C–SiC composites with different fiber architectures. Ceram Int 2015;41(9):12087–98. http://dx.doi.org/10.1016/j.ceramint.2015.06.026.

[24] Raju K, InSubHan, Kim S-H, Kim SY, Seong Y-H. Fabrication of cross-ply Cf/C-SiC composites and the investigation of pyrolysis conditions on their properties. J Ceram Process Res 2020;21(1):113–8. http://dx.doi.org/10.36410/jcpr.2020.21.1.113.

[25] Wich F, Flauder S, Schneider N, Fleck M, Langhof N, Krenkel W, Schafföner S. Processing properties and pyrolysis behavior of novolak-hexamethylenetetramine mixtures. Adv Manuf: Polym Compos Sci 2023;9(1). http://dx.doi.org/10.1080/20550340.2023.2187687.

[26] Mizuno M, Zhu S, Nagano Y, Sakaida Y, Kagawa Y, Watanabe M. Cyclic–fatigue behavior of SiC/SiC composites at room and high temperatures. J Am Ceram Soc 1996;79(12):3065–77. http://dx.doi.org/10.1111/j.1151-2916.1996.tb08078.x.

[27] Niu ZB, Chen SA, Li Y, Xiao P, Yang ZM, Tong YG, Almeida R. A damage constitutive model for the nonlinear mechanical behavior of C/SiC composites during mechanical cyclical loading/unloading. Compos Part A: Appl Sci Manuf 2022;161:107072. http://dx.doi.org/10.1016/j.compositesa.2022.107072.

[28] Evans AG, He MY, Hutchinson JW. Interface debonding and fiber cracking in brittle matrix composites. J Am Ceram Soc 1989;72(12):2300–3. http://dx.doi.org/10.1111/j.1151-2916.1989.tb06079.x.

[29] Lamon J. Influence of interfaces and interphases on the mechanical behavior of fiber–reinforced ceramic matrix composites. In: Bansal NP, Lamon J, editors. Ceramic matrix composites: Materials, modeling and technology. Wiley-VCH; 2015, p. 40–64. http://dx.doi.org/10.1002/9781118832998.ch3.